Average crack front velocity during subcritical fracture propagation in a heterogeneous medium

Olivier Lengliné, Renaud Toussaint, and Jean Schmittbuhl
IPGS, EOST, CNRS, Université de Strasbourg, 5 rue René Descartes, 67084, Strasbourg, France

Jean Elkhoury, J.P. Ampuero
Seismological Laboratory, California Institute of Technology, Pasadena, USA

Ken Tore Tallakstad, Stéphane Santucci, and Knut Jørgen Måløy
Department of Physics, University of Oslo, PB 1048 Blindern, NO-0316 Oslo, Norway
(Dated: April 20, 2011)

We study the average velocity of crack fronts during stable interfacial mode I fracture experiments in a heterogeneous quasi-brittle material under various loading rates, at imposed loading speed or during long relaxation tests, exploring subcritical to critical regimes. Transparency of the material (PMMA) allows to track continuously the front position and to relate its evolution to the energy release rate. Despite significant velocity fluctuations at local scales [1], we show that a model of independent thermally activated sites successfully reproduces the large scale behavior of the crack front for several loading conditions.

I. INTRODUCTION

Fracturing of materials is an important scientific issue that is strongly related to the strength of engineering structures and natural materials such as rocks [2], sea ice [3] and wood [4]. The mechanisms responsible for the onset and evolution of crack propagation are of central importance for the assessment of such failures [5]. In the general context of fracture mechanics, several regimes of behavior are often reported. According to the Griffith energy balance concept, in a quasistatic regime the energy release rate G is roughly constant and equal to a material dependent critical energy release rate, $G \sim G_{gr}$ [6]. This critical energy release rate G_{gr} is the free energy per unit surface area associated with the creation of new crack surfaces. In unstable configurations or during fast loading the kinetic energy becomes important, leading to a dynamic regime [7, 8]. In the slow unstable regime, i.e. at rupture velocity lower than the Rayleigh wave speed, the crack propagation speed is roughly proportional to the difference between G and G_{gr} (e.g. [9]). However, in these brittle regimes, the propagation is strongly controlled by the loading type (imposed stress or imposed displacement), the loading rate and the material rheology. Modeling approaches in these cases are typically based on the LEFM approximation [10].

Rice [11] generalized the Griffith concept of fracture in the framework of irreversible processes (second law of thermodynamics). This formalism introduces some consequence on the kinetic aspects of crack propagation, in particular it allows slow propagation of fracture (much below the Rayleigh wave speed) for energy release rate lower than the Griffith critical energy release rate G_{gr}. In consequence this slow kinetic crack propagation is usually referred to as sub-critical crack growth or subcritical regime. Statistical physics models suggests that this sub-critical regime is governed by a thermally activated mechanism where the strain rate often obeys an Arrhenius law, i.e. corresponds to a Boltzmannian of the gap to a critical energy level, $G_c - G$ [6, 12, 13]. In this approach, the crack growth is directly influenced by environmental factors (applied stress, temperature, chemical concentrations) that are affecting the free energy, and thus the energy barrier, via numerous competing mechanisms like stress corrosion, diffusion, dissolution, plasticity and thermal effects [2, 6]. Experimentally, several empirical relations have been often reported to divide the slow crack propagation in three main characteristic regimes [14]: in a first regime I, at very slow velocity, external variables are dominant and result in an increasing speed of crack growth with increasing G; a weak stress-sensitive regime II follows where transport is limiting. At higher stress, regime III appears and crack growth kinetics become similar to the case without environmental effects. Different kinetic relations other than the Arrhenius law have also been reported to describe the slow crack growth. These relations are generally inferred from fitting an empirical formulation to experimental data on a $G - \bar{v}$ diagram where $\bar{v}$ is the crack velocity. Such relations involve for example, power laws with low exponent [15] or with high exponent when the crack propagation is more sensitive to chemical reaction rate [16, 17]. To simplify the relationship between strain rate (i.e. crack front advance) and stress, some models consider that the crack propagation speed is roughly proportional to the difference between G and an energy release rate threshold, or to a power law of this difference, *i.e.* a Paris' law (e.g. [18–20]). The Arrhenius form of the kinetic fracture evolution is appealing as it has a certain universality (associated to statistical mechanics), is related to any thermally activated mechanism at the molecular scale, can deal with the stress dependence of such mechanism, and can be derived from first principles, as the theory of process rates[6]. Such a relation is also supported by

experimental data [2, 21] and if the dependence of the free energy G on the strain can be adequately linearized, a logarithmic time dependence of the strain, and of the force, can be derived. This is observed for many creeping systems, as e.g. in different granular systems displaying a time logarithmic deformation (or force) during the slow relaxation [22–24].

For heterogeneous materials, crack propagation is however influenced by local variations of the material properties, micro-structures, thermal fluctuations, development of a process zone, etc [25]. The interplay of the different contributions to the crack growth makes its analysis a complex problem. It is indeed difficult to discriminate the part of each contribution observing the evolution of a crack advance at a microscopic level. In terms of macroscopic strength, the failure of brittle materials with weak flaws are typically described by Weibull statistics of the flaw strengths which rely on the weakest-link approach and extreme-value statistics [26]. A departure from this class of materials is exhibited by quasibrittle materials for which ductile behavior around the crack tip imposes an elementary representative volume of non negligible size compared to the sample size. These materials show significant scaling or size effects in particular at very low loading rates [27]. The question of possible intermediate scales between the microscopic flaw scales and the sample scale when brittle and ductile local rheologies are competing, is an active field of research. In particular when time effects come into play the former regime being dominated for processes in series, the latter for processes in parallel, depending on the loading geometry [28, 29].

The interfacial crack propagation configuration has long been a favorable experimental situation for fine monitoring of crack propagation. It consists of a single cantilever beam configuration with a propagation along a weak interface. For brittle material like mica, it was the first setup to enable measurements of fracture energy [30]. In the case of quasibrittle materials (*e.g.* PMMA), it provided the first detailed observation of the morphology of the crack front [31, 32]. This makes it possible to measure the distribution of the local velocities of the crack front, which display at small scales an intermittent behavior [1, 33]. Recently, the impact of the loading regime on the local dynamics of the crack was investigated [33]. It was found that the scaling properties of the crack front remain unchanged in both high and slow speed limits, suggesting that a common mechanism might be operating in these two regimes. This was the case both for the front geometrical properties (scaling of the front roughness), and for the time and space scaling properties of the velocity fluctuations. The interfacial configuration is also favorable for numerical simulations since it reduces the roughening of the crack front to an in-plane problem. Two modeling approaches are followed: a microscopic description of the crack front as a continuous line [9, 34–36] and fiber bundel models in which a discrete population of active sites are competing under various interaction rules [37–41].

We focus here on the experimental description of the spatially averaged velocity of the crack front in the interfacial fracture configuration, under various loading conditions, at the transition between sub-critical and critical propagation. Our heterogeneous medium consists of an interface between two PMMA plates with small toughness fluctuations [42]. Each local asperity is the site of a depinning transition which leads to a progressive local advance of the crack front. By taking advantage of the transparency of our sample, we obtain a direct optical monitoring of the global evolution of the crack. Two types of loading are explored: low imposed loading speed (up to 1 mm/s) and relaxation test at fixed load point displacement. In both loading regimes, we compare the average crack velocity to the loading velocity or the energy release rate. In a second part of the manuscript, we show that the large scale evolution of the crack front velocity can be explained by a simple model of a population of statistically independent but temperature sensitive microscopic active sites, slowly evolving, *i.e.* following an Arrhenius law. This assumption will be checked by comparing this simple model with experimental data. Numerical solutions of the model correctly describe the experimental behaviors for time scales spanning over 6 orders of magnitude and for both loading types. The determination of the parameters of this subcritical crack growth law from the experimental data, allows to determine a characteristic size of the individual breaking bonds in this material around $10^{-11}\,m$, a scale comparable to the separation of individual molecular elements but below the scaling range of the crack front (10μm to 10mm), similar to the scales determined for granite [43] or for paper [44] and numerous materials [13].

In addition to the numerical solutions of the full equations, simple analytical expressions of the front position evolution in these two regimes (imposed loading speed or relaxation) are derived under several approximations. Notably, a slow time-logarithmic relaxation is found, and its parameters are interpreted. Another result of this numerical treatment is that the Griffith regime, for which at imposed loading velocity stays roughly constant, $G \sim G_{gr}$, is derived as a result: it is to be a particular case, for large enough loading velocities, resulting from the Arrhenius law with stress activated microscopic sites and linear elasticity describing the dependence of the stress on the large scale geometry.

II. EXPERIMENTAL ANALYSIS

A. Sample Preparation

We use two transparent polymethylmethacrylate (PMMA) plates, one narrower than the other, to prepare our transparent sample. The dimensions of the plates are $20\,cm \times 10\,cm \times 1,0\,cm$ and $23\,cm \times 2,6\,cm \times 0,5\,cm$ respectively for the large and the narrow plate. First, we sandblast one surface of the narrower plate with glass

beads of diameter ϕ ($\phi \in [180 - 300]\,\mu m$). The blasted plate is cleaned to remove any electrically attached glass beads. Then we assemble the two plates in a stiff aluminium frame with the blasted surface facing a surface of the larger plate. Finally, we subject the assembled plates to a homogeneous normal load of 3 MPa and heat the assembly in an oven at $190°C$ for 45 minutes to anneal the plates. The thermal annealing produces a cohesive interface that is weaker than the bulk and constrains the sample to break in mode I along the prescribed interface. The glass bead blasting introduces random heterogeneities in the surface topography that provides surface roughness and controls the local strength at the interface. The induced microstructure at the interface makes the sample opaque, but the newly formed block, after annealing, recovers its transparency since contrast of the refraction index along the interface disappears.

B. Acquisition and Image Processing

Once the sample is ready, we clamp the large plate to a stiff aluminium frame. A stepping motor applies the loading over the tip of the narrow plate in a direction normal to the plate surface (see Figure 1). The contact on the plate is imposed by a freely rotating rod (using ball bearing), made of a low friction coefficient material (polyamide PA 6.6). This implies that a minimum shear force is actually acting on the loaded plate which prevents mode II loading of the fracture tip. We measure the vertical displacement at the loading point with a linear variable differential transformer (LVDT) and the force load by an STC 1205 traction/compression transducer. Displacement and force are measured with a resolution of $1,3\,\mu m$ and $2,4 \cdot 10^{-3} N$ respectively. The vertical displacement imposed on the narrower sample induces the stable propagation of a mode I planar fracture along the prescribed interface. The loading velocity varies for each experiment within the range $[6\,\mu m \cdot s^{-1}; 600\,\mu m \cdot s^{-1}]$ and is zero during creep tests. This leads to null front velocity at the start of experiments and maximum front velocities of the order of $3 \cdot 10^3 \mu m \cdot s^{-1}$. The total advance of the crack front achieved during an experiment is typically of the order of $1\,cm$.

We monitor the fracture front by optical means. A camera (Nikon D700) with up to ~ 5 frames per second is used to follow the crack front propagation. The images have a dimension of 4256×2832 pixels and the resolution is in the range of $5 - 10\,\mu m/pixel$. Figure (1) represents a scheme of the experimental setup configuration. Optical images of the interfacial mode I rupture are divided in bright and dark regions representing respectively the cracked open and unbroken sections of the sample. Image processing aims at obtaining the transition between the bright and dark areas of the images representing the transition between the broken and unbroken regions that define the fracture front. We first compute the difference of the graymaps between each image and the first image of the experiment. This first step highlights the difference at the two stages of the fracture process while removing permanent artifacts associated to index variations in the material. Then, grayscale images are transformed into black and white images according to a threshold value which represents the gray level separation between the bright and dark regions. The gradient of this last image is used to extract the largest cluster of connected pixels with non-zero gradient, which are assumed to represent the front position, $a(x,t)$. The front propagates on average along the y axis where the origin is defined at the free end of the plate and is positive in the direction of propagation of the crack. The x axis is perpendicular to the y axis and defines the coordinate of a point along the front. t is the time, and $a(x,t)$ is the y position of the front at lateral position x and time t. We compute from each profile the average front position $\bar{a}(t)$. For a more complete description of the image processing, see references [1, 42].

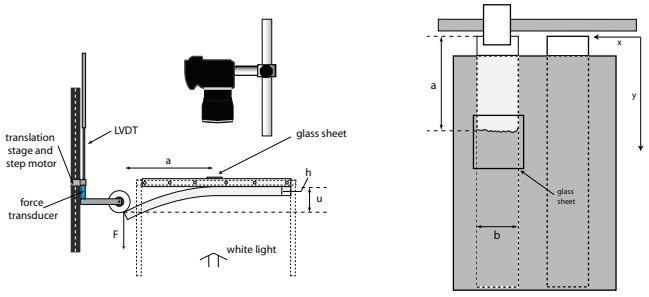

FIG. 1: Side view (left) and top view (right) of the experimental setup. A stiff aluminium frame is attached to the upper PMMA plate. The bottom plate is separated from the upper one by a load F applied by a rod connected to a stepping motor. The rod can freely rotate around its axis. The load causes a deflection u of the bottom plate and the propagation of a mode I crack. The crack front is located at the averaged distance $\bar{a}$ from the free end ($\bar{a}$ is obtained by the spatial average of the distance a along the front). Front advance is monitored by a camera set in vertical position, perpendicular to the crack plane. We add glycerol between the upper plate and a thin glass sheet located above the crack front to enhance the optical contrast of the pictures. The narrow plate thickness and width are noted h and b respectively.

C. Typical Run of an Experiment

All the experiments start with no initial deflection, i.e. the loading point is not in contact with the narrow PMMA plate. The stepping motor then produces the vertical displacement of the loading point at controlled speed V_l. Once contact is achieved between the loading point and the plate, the force, F, at the free end of the plate increases as well as the deflection, u. The force increase leads to the initiation of the crack movement while the loading point continues to move downward at constant velocity. The amount of time spent in this constant load-

ing velocity regime is inversely proportional to V_l. The step motor is then stopped, i.e. $V_l = 0$, at $t = t_{stop}$ leading to a decrease of the crack front speed, which is monitored typically for 5 minutes but reaches up to more than 18 hours in one experiment. The sample is finally unloaded by moving the loading point upward back to its initial position, leading to arrest of the front. The next experiment starts where the previous one ends until the front reaches the end of the plate. All experiments where carried out at room temperature ($T \in [22, 2-24, 4]C^o$). These experiments were carried out on two completely independent setups by different experimentalists, with no noticeable discrepancies between the results.

An example of a typical experiment is displayed on Figure 2. The sample is loaded continuously with a velocity of $62\,\mu m.s^{-1}$ during 230 seconds. The rupture initiates at $t \sim 190\,s$ as evidenced by the onset of the front movement and by the deviation of the force from a linear trend. As long as the sample is continuously loaded we observe an increase of the crack velocity. The loading point is then maintained at fixed deflection at time $t_{stop} = 230\,s$ as indicated by the vertical gray line. As the loading point velocity is set to zero, the front velocity exhibits a deceleration during the entire recording period (5 minutes) while the force is also continuously decreasing. All the experiments where carried following the same scheme as presented in Figure 2, and different loading velocities were tested $V_l \in [6; 600]\mu m.s^{-1}$.

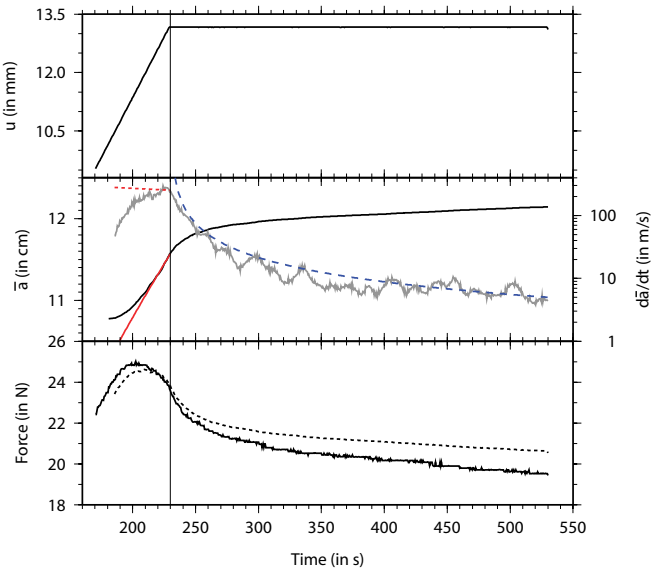

FIG. 2: Top : Variation of loading point position, u, as a function of time during an experiment. At time $t = 230\,s$, the loading point is maintained in a fixed position. Middle: Variation of the average front position, $\bar{a}$, as a function of time (black solid line) and evolution of the crack front velocity $d\bar{a}/dt$ (gray solid line). The red solid and dashed lines represents a fit to the average front position and velocity, respectively, according to Eq. (18). The blue dashed line is a fit to the crack velocity in the relaxation regime following Eq. (25). Bottom : Variation of force as a function of time (black solid line) and force predicted by the beam theory (dark dashed line) using (5) with $E = 3.2\,GPa$, $h = 4.9\,mm$ and $b = 2.84\,cm$ which are the measured properties of the plate. For all figures, the vertical gray line denotes the time at which the loading was stopped and separates the imposed velocity regime from the relaxation regime.

III. EXPERIMENTAL OBSERVATIONS

We separately describe our observations of the crack propagation in the two loading regimes, at constant loading velocity, or at contant loading position. We will report here the behavior of the average front position with time, and show that they follow simple laws. In the following section, we will derive these laws on a theoretical basis, and interpret physically their parameters.

A. Constant Loading Velocity

We first focus on the regime with constant loading velocity, V_l. As observed in Figure 2 an initiation phase precedes the propagation of the crack at an almost constant velocity. We display on Figure 3 the evolution of the front position as a function of the loading point displacement, u. For each experiment we keep only data points with $t < t_{stop}$, i.e. the dynamics of the crack is supposedly driven by the applied load at constant velocity. For each sample we observe that the evolution of $\bar{a}$ can be well approximated by a fit of the form $\bar{a}(u) \propto \sqrt{u}$, as evidenced by the fits on Figure 3.

B. Constant Deflection Condition

We now turn to the relaxation regime characterized by a constant deflection u, which occurred when $t > t_{stop}$. We observe in Figure 2 a progressive deceleration of the front. In order to precisely describe the evolution of the front position in this particular regime we set $\bar{a}_0 = \bar{a}(t_{stop})$ and we represent the evolution of the front position $\bar{a}(t) - \bar{a}_0$ with time since t_{stop} for several experiments. We observe that data, displayed on Figure 4, shows a logarithmic evolution of the front advance for large times (corresponding to a linear behavior in this semilogarithmic representation). We propose to fit the advance of the front by a logarithmic relation of the form

$$\bar{a}(t - t_{stop}) - \bar{a}_0 = A \ln\left(\frac{t - t_{stop}}{t^*} + 1\right), \qquad (1)$$

where t^* is a characteristic time and A an empirical constant with dimension of length. We observe on Figure 4 that Eq. (1) provides a good fit to the observed data. We obtain typical values of t^* of the order of $1 - 10\,s$ while

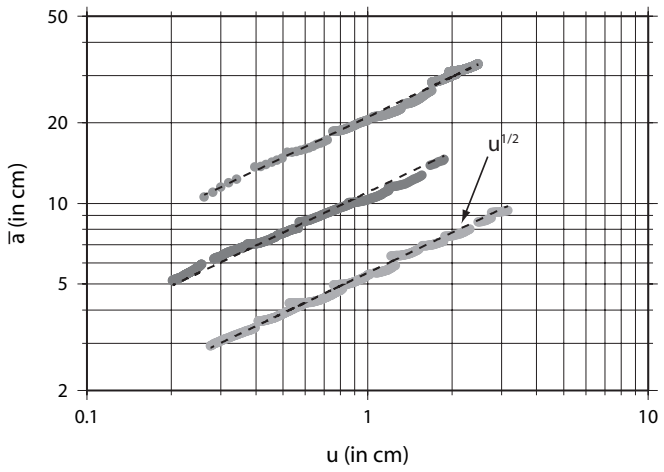

FIG. 3: Variation of the crack front position, $\bar{a}$, as a function of the loading point displacement, u. The gray points refer to recorded data from different samples. For each sample we carried several experiments. The best fit using $\bar{a}(u) \propto u^{1/2}$ is displayed as a black line for each sample. Crack front positions are shifted vertically for each sample in order to enhance the visibility (by a prefactor corresponding respectively to a factor 0.5 for the lowest and 2 for the highest curves). We see that for each sample and for each experiment the observed behavior is in good agreement with the fitted trend. One can notice however that the crack initiation does not seem well approximated by this trend.

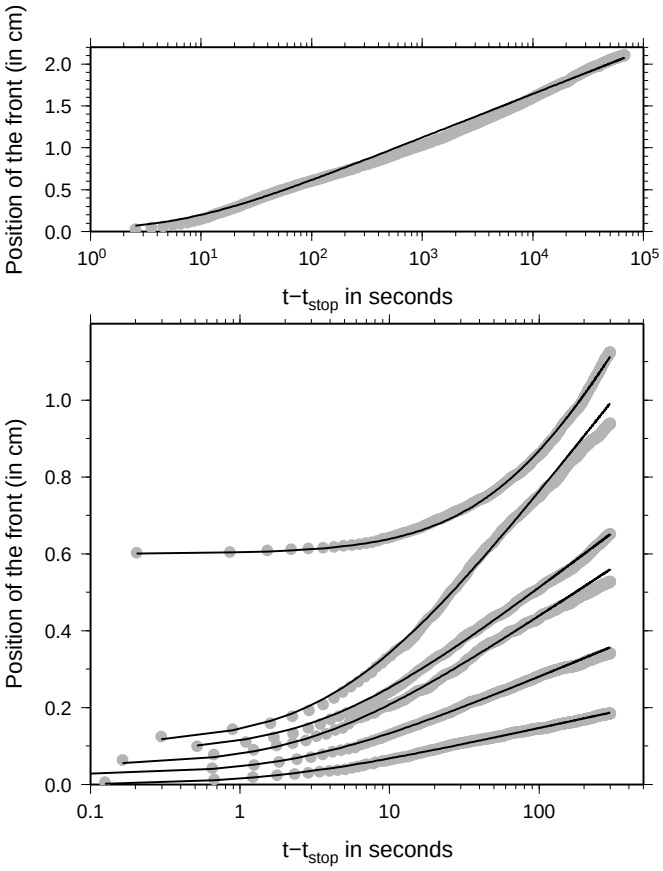

FIG. 4: Evolution of the average front position $\bar{a}(t) - \bar{a}_0$ during several relaxation experiments as a function of time $t - t_{stop}$. The observed front position is represented by gray dots while the best fits using (1) are displayed as continuous dark lines. Traces have been shifted vertically in order to enhance visibility. The experiment displayed on the top figure lasted more than 18 hours (the time representation scale is different from the one in the bottom figure).

typical values of A are of the order of $10^{-4} - 10^{-3}\, m$. We also report on Figure 4 the evolution of the front position during this relaxation regime for an experiment which lasted more than 18 hours in such a regime. We apply the same fit (Eq. 1) to these data and we still observe a reasonable agreement. Indeed, no clear deviation from the logarithmic behavior is observed. Even in this long term experiment, the propagation of the front remains small ($\sim 2\, cm$). This logarithmic evolution of the crack front contrasts with the previous one found in the regime at constant loading velocity. The large-scale progression of the front must be dominated by a process capable of capturing such distinct behaviors.

IV. A SUBCRITICAL CRACK PROPAGATION MODEL

A. A Thermally Activated Microscopic Process

We suppose that the crack propagation is governed at the local scale, by a subcritical mechanism following an Arrhenius law [15]. Owing to thermal fluctuations large enough to overcome the fracture energy barrier of individual bonds the fracture is allowed to propagate at slow speed. This contrasts with the Griffith approach where no propagation is allowed below the Griffith energy release rate G_{gr} (or below the Griffith stress intensity factor K_{gr} following an Irwin criterion [6]). The fracture energy barrier is supposed to be fluctuating in space but constant on a characteristic microscopic scale α which is a length scale associated to the individual degrees of freedom of the microscopic fracturing process. At zero loading, we consider that the magnitude of the barrier is related to the local critical energy release rate: $\alpha^2 G_c$. This aspect of a quenched fluctuating zero-loading barrier relates material properties to G_c, and the energy gap to reach it is also dependent on the the elastical mechanical energy around the crack tip which is described by the local energy release rate $\alpha^2 G$. Such a model coupling thermal noise and spatial disorder have been previously investigated in some theoretical approaches in fiber bundle models or irreversible crack growth model [45, 46]. We note $\Delta G = G_c - G$ the difference between the local energy release rate, G, and the local critical energy release rate or fracture energy, G_c. The probability for an individual asperity to go beyond this barrier, per period characteristic of the microscopic thermal motion, τ_B, is introduced as a Boltzmannian of the relative elastic en-

ergy $\alpha^2\Delta G$. The Arrhenius relation governing the local fracture velocity $v = da/dt$ can thus be written as:

$$v(G, G_c) = \psi \exp(-\alpha^2 \Delta G/k_B T), \tag{2}$$

where ψ is a constant of proportionality equal to α/τ_B, T is the absolute temperature (in Kelvin), k_B is the Boltzmann constant.

B. A population of Independent Microscopic Sites

We propose a model for the average crack velocity based on a statistical approach. The behavior of the weak interface is assumed to be dominated at large scales by a discrete set of independent microscopic sites. The large-scale evolution law of the crack front speed is obtained by integrating Eq. (2) over all local microscopic sites at a given time. Such an integration is not straightforward as there might exist correlations among local values of G and G_c. Fluctuations in G are resulting from the crack front roughening around its average position $\bar{a}$ [34] and a perpendicular, large scale, stress gradient owing to the bending of the loading plate. For the fracture energy, G_c, the quenched fluctuations result from the sample preparation. Such fluctuations introduce correlation over a finite length of local velocities [33]. We will hypothesize that at the macroscopic scale, above these correlation lengths, the average (or large-scale) evolution of the front is governed by a law similar to (2) but involving only large scale average quantities $\bar{G}$ (describing the average loading along the front) and $\bar{G}_c$ (describing the upscaled energy barrier at the front scale) - the critical size of the degree of freedom, α, being preserved. For example in an (over-)simplistic model where all parameters would be statistically independent and where G and G_c could be described by two independent normal distributions with respective mean $\bar{G}$ and $\bar{G}_c$ and root mean square σ_G and σ_{G_c}, we would get

$$\bar{v} = \chi \exp(-\alpha^2(\bar{G}_c - \bar{G})/k_B T), \tag{3}$$

where $\chi = \psi \exp\left[\frac{\alpha^4(\sigma_G^2+\sigma_{G_c}^2)}{2k_B^2T^2}\right]$.

We acknowledge that at small scale, parameters as G and G_c are not statistically independent and that intermittent behavior, large fluctuations of velocity, and the spatial correlations in G and in G_c have been described in details (e.g. [1, 33]). We nevertheless assume that the upscaling leads to a simple form as in Eq. 3. Such an upscaling could result from the existence of a discretization scale above which asperities could be considered independent. This discretization scale could be analogous to the representative elementary volume (REV) introduced by Bažant and Pang [29] for quasi-brittle materials. Within each REV, the effective failure of the asperity is considered as a purely thermally activated and stress dependent process. This model is not continuous contrary to contact line approaches [9, 34–36]. It can rather be compared to fiber bundle models [37–41] or interacting damage models [47–50] but with a non-direct stress redistribution.

At this stage, to describe the dynamics of the upscaled (spatially averaged) velocity, mechanical interactions between microscopic sites are ignored for simplicity, and we hypothesize that only the mechanical energy release rate controlling the upscaled velocity depends mostly on the large scale average front position, which is essentially flat at large scales – i.e. we postulate that the upscaling of Eq. (2) leads to a similar form, with only upscaled energy released rates and energy barrier, Eq. (3). This strong assumption will be checked by comparing this very simple model and the experimental data. It will be shown to hold, not only for the relaxation regime, but somehow more surprisingly, also for the forced regime.

C. A cantilever configuration

The average energy release rate $\bar{G}$ is estimated from a classical elastic plate theory neglecting the fluctuation of the front position around a mean flat front $\bar{a}$. During the experiment, the average energy release rate can accordingly be computed from the elastic strain energy, U_E, stored in the loading plate as:

$$\bar{G} = -\frac{1}{b}\frac{dU_E}{d\bar{a}}, \tag{4}$$

where b is the width of the plate and $\bar{a}$ is the average crack front position [6]. From 1D beam theory a linear relation exists between the applied force, F, and the deflection of the beam, u,

$$F = \frac{uEbh^3}{4\bar{a}^3}, \tag{5}$$

where E and h are respectively the Young modulus and the thickness of the narrow plate [6]. This leads to the following expression of the elastic energy

$$U_E = F\frac{u}{2}. \tag{6}$$

Combining Eqs. (4), (5) and (6) finally leads to an estimation of the average energy release rate in our system

$$\bar{G} = \frac{3u^2Eh^3}{8\bar{a}^4}. \tag{7}$$

D. A macroscopic evolution law

By combining Eqs. (3) and (7), we can derive the complete expression of the evolution of the crack front velocity:

$$\bar{v} = \frac{d\bar{a}}{dt} = \chi \exp\left(\frac{\alpha^2}{k_B T}\left[\frac{3u^2Eh^3}{8\bar{a}^4} - \bar{G}_c\right]\right). \tag{8}$$

Eq. (8) is the differential equation that governs the movement of the front in our experimental configuration. This equation takes different forms depending on the loading scheme, which manifests in the expression of the time-dependent imposed deflection, $u(t)$. We explored the two particular loading conditions imposed on the experimental system, namely a constant loading velocity condition and a fixed deflection condition.

As a first check, we computed the average crack front velocity, $\bar{v}(t)$. This is obtained by smoothing $\bar{a}(t)$ values with a window running along time and then dividing each incremental position by the time interval between successive pictures. We estimate $\bar{G}$ at each time interval from Eq. (7). We represent on Figure 5a the average crack front velocity as a function of the average energy relase rate $\bar{G}$ computed from Eq. (7) for 13 experiments. We see that a linear relationship ($\log(v)$ vs G) is a good proxi of the whole behavior of each experiment where the sample undegoes multiple loadings: first a constant loading velocity condition followed by a constant deflection condition. To account for the horizontal shift in G between experiments, we searched for an estimate of $\bar{G}_c$ for each experiment following Eq. (3):

$$\ln(\bar{v}) = \ln(\chi) + \frac{\alpha^2}{k_B T}(\bar{G} - \bar{G}_c), \qquad (9)$$

that provides the best superimposition of all experimental curves (see Figure 5b). Deduced values of $\bar{G}_c$ are reported in Table I. We used $k_B = 1.38 \cdot 10^{-23} J \cdot K^{-1}$, $T = 300K$ and obtained the value of α by least square fitting: $\alpha = 25pm$. The characteristic length scale α at which the elementary fracturing process is expected to occur is thus of the order of $10^{-11}m$. This implies that the rupture process is governed by mechanisms operating at the scale of the bond distance between atoms. This is consistent with the physical picture underlying the Arrhenius law, where each individual degree of freedom in the system can break with a certain probability set by thermodynamics to be a Boltzmann distribution: we find that these individual degrees of freedom probably correspond to individual molecules crossing through the weak interface.

We see from Table I that the fracture energy $\bar{G}_c$ has a median value of 200 $J \cdot m^{-2}$ with 20% fluctuation. Such a range of variation is compatible with sample preparation variability (plate thickness fluctuation, non fully homogeneous annealing procedure, sand-blasting variability, etc) and are very consistent with results obtained in [51].

Other relations linking the crack speed to the energy release rate have been proposed as $\bar{v} \sim e^{-E'/k_B T} G^{n/2}$ [16], or transforming ΔG in (3) into $\Delta G^{-\mu}$, where the exponent μ arises from possible 3D paths taken by the crack [43, 52]. Our experimental data do not allow us to discriminate confidently among these different formulations. The simple Arrhenius law introduded in Eq. (3) where the energy barrier is linearly related to the difference between G and G_c can be considered as a relevant model of the fracture process within each microscopic site

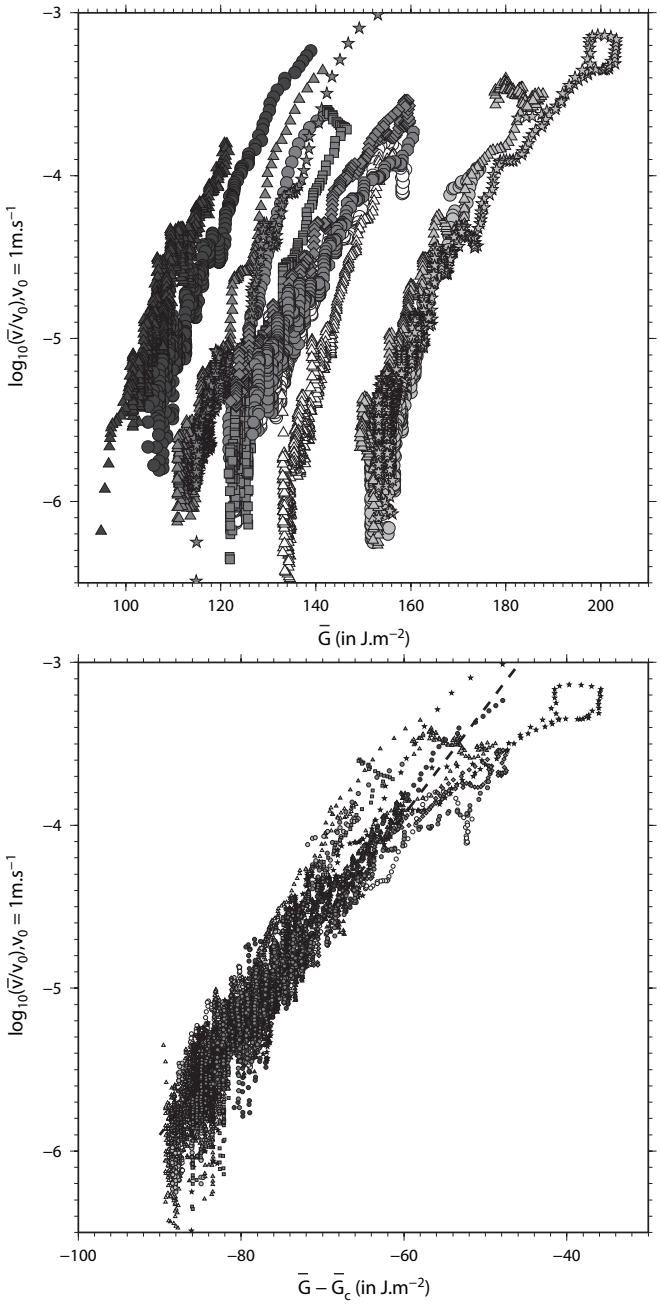

FIG. 5: a) Variation of the logarithm of the average crack front velocity as a function of the average energy release rate. All experiments are reported in this figure and are distinguished by gray levels and symbols. For each experiment, both loading regimes (constant loading velocity and relaxation regimes) are included. Similar gray levels indicate experiments performed in the same region of one specific plate (short separation distance between fracture onsets). b) Superimposition of all experiments when plotting as a function of: $\bar{G} - \bar{G}_c$. Values of $\bar{G}_c$ are computed for each experiment assuming $\alpha = 25pm$ and $\chi = 1m.s^{-1}$. The dashed curve represents the best fitted model.

in our experiments. Indeed it fits nicely the experimental data over several orders of magnitude of average crack

TABLE I: Values of $\bar{G}_c$ determined by fitting (9) to our experiments and imposing the same value of α for all experiments. The best least square estimate of α yields $\alpha = 25pm$. The corresponding values of v_1 computed from Eq. 10 and imposing $\chi = 1m \cdot s^{-1}$ are also reported.

Experiment	$\bar{G}_c$	v_1 in $m.s^{-1}$
1	210	$2 \cdot 10^{-14}$
2	222	$3 \cdot 10^{-15}$
3	240	$2 \cdot 10^{-16}$
4	236	$3 \cdot 10^{-16}$
5	239	$2 \cdot 10^{-16}$
6	186	$6 \cdot 10^{-13}$
7	181	$1 \cdot 10^{-12}$
8	202	$6 \cdot 10^{-14}$
9	199	$8 \cdot 10^{-14}$
10	200	$7 \cdot 10^{-14}$
11	208	$2 \cdot 10^{-14}$
12	207	$3 \cdot 10^{-14}$
13	210	$2 \cdot 10^{-14}$

speed, as shown in Figure 5.

V. NUMERICAL SOLUTIONS

We propose to solve numerically the Arrhenius law, Eq. (3), with the prescribed loading and dependence of $\bar{G}$ on $\bar{a}$ and u, Eq. (8), in order to obtain predictions of the evolution, for each experiment, of the front position, the loading force and the energy release rate. This allows a second check of the validity of the activated energy mechanism introduced to describe the crack front propagation. Unfortunately setting $u = V_l \times t$ or $u = const.$ in Eq. (8) does not lead to analytical solutions.

We first introduce a characteristic speed v_1 defined as:

$$v_1 = \chi \exp\left(-\frac{\alpha^2 \bar{G}_c}{k_B T}\right). \tag{10}$$

As a second step, we show that Eq. (8) can actually be rewritten in a much simpler form by introducing dimensionless variables: $\bar{a}' = \bar{a}/\lambda$ and $t' = t/\tau$. In the *forced regime* where $u = V_l t$, we introduce:

$$\lambda = \alpha \frac{V_l}{v_1}\left(\frac{3Eh^3}{8k_B T}\right)^{1/2} \tag{11}$$

$$\tau = \frac{\lambda}{v_1}, \tag{12}$$

which leads to:

$$\frac{d\bar{a}'}{dt'} = \exp\left(\frac{t'^2}{\bar{a}'^4}\right). \tag{13}$$

The values of the force, in our model, are computed from the front position using Eq. (5). Eq. (5) is solved numerically using a simple Euler model with a constant time step. We found that the evolution of $\bar{a}$ and F can both be well reproduced as a solution of Eq. (13) when setting $\alpha = 25pm$ and $v_1 = 1.0 \cdot 10^{-14} m.s^{-1}$. These values fall in the range of parameters estimated from table I and represent acceptable results. We should note however that these two parameters are not very well constrained as they are highly correlated such that a change of α can be balanced by a change of v_1. We see on Figure 6 the evolution of force, front position and $\bar{G}$, for six experiments as well as the results of the numerical integration of Eq. (13). All six experiments are carried on the same plate. In the forced regime, the loading velocity is $V_l = 310\,\mu m.s^{-1}$ for the first three experiments and $V_l = 62\,\mu m.s^{-1}$ for the last three experiments. The width of the plate is $2.84\,cm$, its thickness is $h = 4.9\,mm$ and the Young modulus of the PMMA plate is $E = 3.2\,GPa$. All solutions with a common loading velocity tend to align on the same curve after a sufficiently long time. This results from the common time dependence of equation (13) in all experiments with the same loading velocity. Differences arise from the variation of the initial front position at the start of the experiment. We see on Figure 6 that our numerical model, resulting from the coupling of the cantilever beam configuration of our system and the activated energy mechanism necessary to describe the fracture process, is in good agreement with the evolution of the force, front position and energy release rate.

Interestingly, we note that the integration of this thermal activation model with the large scale elastic mechanics, over these characteristic time scales, with a constant velocity loading, leads to roughly constant values of G during the propagation: this means that the fact that $G\ cst$, i.e. a Griffith regime for the fast propagation, results from the direct integration of this subcritical model with a proper forcing in the evaluation of G.

It should be noted that the results of the numerical model is dependent on several parameters (e.g. E, b, h) which are affected by some uncertainties such that it could be possible to improve the fits by varying these parameters within their uncertainties range. However the discrepancy between the model and the data is small and could also be the result of second order effects affecting the crack propagation (e.g. viscoelastic effects).

We now turn to the *relaxation regime*, in which the beam deflection is constant. We observe an evolution of the front position in this regime (Figure 4) which is a priori not compatible with LEFM theory and the viscous rheology model as used in simulations e.g by Bonamy *et al.* [53], where it is assumed that the transition to zero propagation velocity of the front is sharp when the energy release rate is below the critical energy for fracture propagation (Griffith criterion, zero temperature limit). The evolution of the crack front in this relaxation regime predicted by our model is obtained by setting $u_{stop} = V_l \cdot t_{stop}$ in (8) and solving the differential equation. In order to solve this equation we rewrite it with the dimensionless variables a' and t' but with:

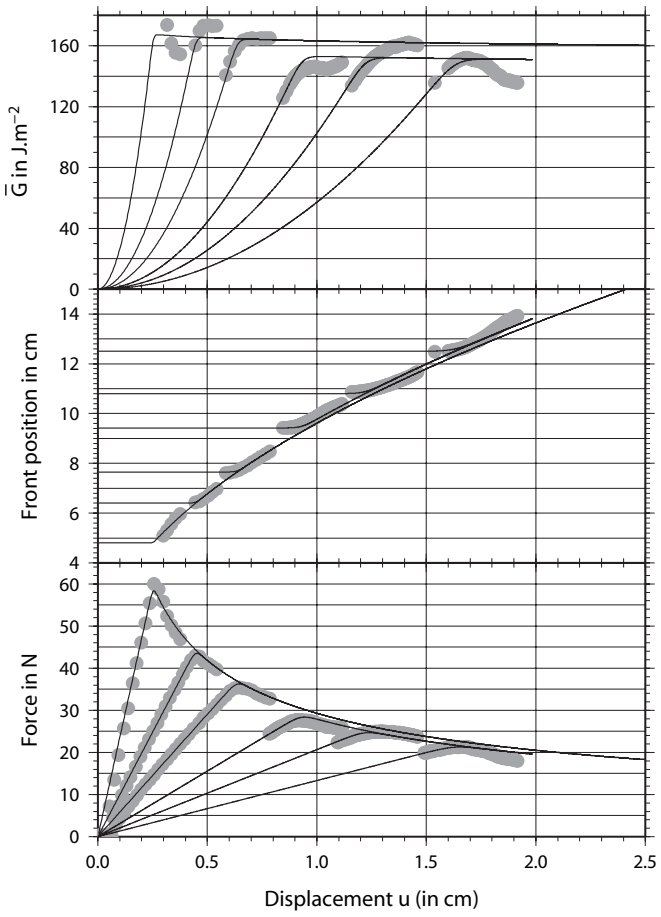

FIG. 6: Variation of force, F, front position $\bar{a}$ and energy release rate, $\bar{G}$, obtained during six experiments (gray points) carried in the forced regime. The results of the numerical integration of Eq. (13) are drawn as black lines. The model captures most of the features observed in our experiments, such as the peak value of the force and its occurrence time. It also captures the appearance of a Griffith regime, i.e. the fact that $\bar{G}$ is close to constant at large enough crack speed.

$$\lambda = \left(\frac{3Eh^3\alpha^2 u_{stop}^2}{8k_BT}\right)^{1/4}, \tag{14}$$

$$\tau = \frac{\lambda}{v_1}, \tag{15}$$

leading to:

$$\frac{d\bar{a}'}{dt'} = \exp\left(\frac{1}{\bar{a}'^4}\right). \tag{16}$$

In order to solve Eq. (16) we keep the same estimate of α and v_1 that were obtained in the constant loading velocity regime. We compare the results of the integration of Eq. (16) with the observed data in the experiment shown in Figure 2. We represent on Figure 7 the evolution of the force and front position from the experimental data and the numerical model. The fit to the front position provided by the integration of (16) is in close agreement with the observed values. In order to detect any long term deviation we also fit our numerical model to the long run experiment (18 hours of relaxation). As this experiment was performed on a different sample we also computed v_1 and α for this experiment. We show in Figure 7 our best fit which is obtained when setting $\alpha = 18pm$ and $v_1 = 5 \cdot 10^{-9} m.s^{-1}$. Both force and front position are well reproduced by the numerical model (dark continuous line in Figure 7A and 7B). We may however observe that at long time scale, the front position (gray dots in Figure 7B) departs from the computed position (dark continuous line in Figure 7B). This may imply that additional processes are taking place affecting the front propagation or that some parameters, considered as constant, did actually vary over the course of this experiment, for instance temperature or broad scale variation of the fracture toughness.

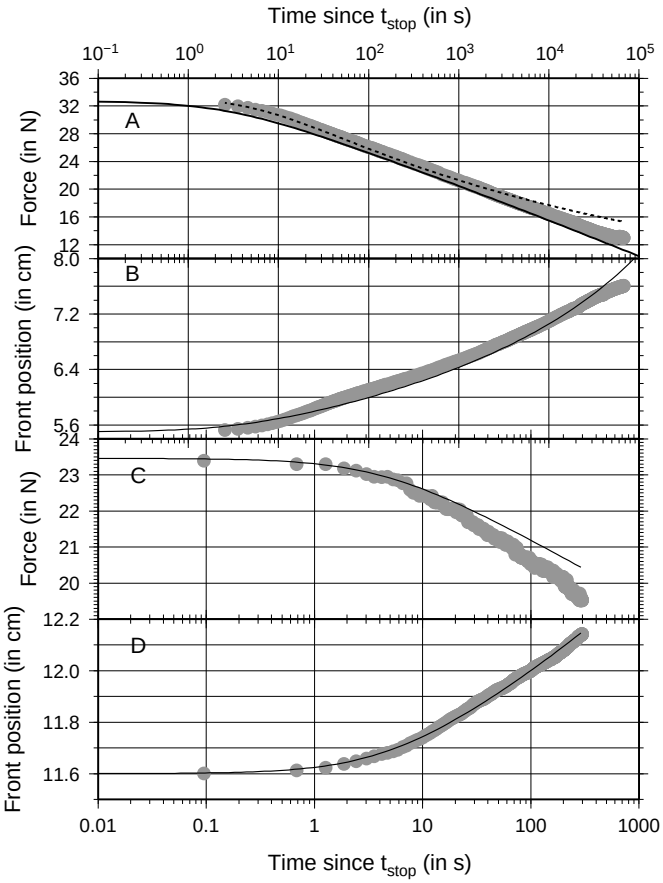

FIG. 7: Variation of force, F and front position $\bar{a}$ obtained during the relaxation regime for the experiment displayed on Figure 2 and for 5 minutes (gray dots, C and D). Results of the numerical integration are represented as black line. Same representation is made for the experiments monitored for more than 18 hours in the relaxation regime and is displayed in the two upper graphs (A and B). The dashed line shows the evolution of force deduced from the fit of the front position from Eq. 1.

VI. DISCUSSIONS

Eq. (8) which governs the large scale motion of the crack has no analytical solution for the two loading regimes investigated in our experiments. However we show that two kinds of simple approximation can lead to analytical expressions of the front advance in close agreement with our experimental observations.

A. A Constant G approximation

We focus here on the case where the energy release rate can be considered as constant: $\bar{G} = const.$ From Eq. (3) this condition should correspond to a constant crack velocity $\bar{v} = const.$ We see actually from Figure 2b that after an initiation phase the propagation of the front is reaching a quasi-constant velocity during the forced regime (when the loading velocity is non zero and constant: $V_l \neq 0$). The initiation phase is expected as the front velocity cannot jump instantaneously from zero to its steady state velocity. This observation supports the assumption that, to first order, during the forced regime the energy release rate, $\bar{G}$, remains the same: $\bar{G} = G_0$ during the crack propagation.

If the energy release rate G is constant we derive from Eq. (7):

$$\bar{G} = \frac{3E\delta^3}{8}\frac{u^2}{\bar{a}^4} = G_0 = const. \tag{17}$$

Introducing $A = \left(\frac{3E\delta^3}{8G_0}\right)^{1/4}$ we get:

$$\bar{a}(u) = A \cdot u^{1/2}. \tag{18}$$

Therefore a constant energy release rate implies a scaling between the average front position $\bar{a}$ and the deflection u. Actually Eq. (18) is the form of the fit used in Figure 3 which shows a good agreement with the experimental data. It thus provides a physical basis to the empirical relation proposed to fit the data.

On the other hand, the result of Eq. (18) in our experiments implies that $\bar{v}(t) \propto V_l/\bar{a}$ as $u \propto V_l t$ in the forced regime. This suggests that the front velocity is decreasing at constant G as the crack front advances although we assumed a constant velocity. However as the evolution of $\bar{a}$ is small around the initial front position for each incremental experiment along the same sample, the evolution of speed $\bar{v}$ is small as well. An evolution between experiments might however exist. Finally, it is noticeable in Figure 6 that the experimental evolution of the energy release rate, $\bar{G}$, is almost constant for the whole duration of the investigated range after an initiation period well reproduced by the complete numerical integration of the Arrhenius law (Eq. 8). This is also in agreement with the hypothesis made that $\bar{G} = const.$ in this forced regime.

B. A First Order approximation of G evolution

We now aim at characterizing the relaxation process which takes place at $t > t_{stop}$. We recall that during this time interval, the loading velocity is zero: $V_l = 0$. From Fig. 2 we find that above t_{stop}, the measured force decreases with time while the average position of the front continues to increase with time. We also observe that this increase of front position is well approximated by a logarithmic evolution as seen in Fig. 4. As Eq. (8) is not tractable analytically in this relaxation regime, we analyze a first order approximation of the solution. Assuming that the evolution of $\bar{a}(t)$ with time is very small in this relaxation regime, we derive a first order expansion of $\bar{G}$ around some position $\bar{a}_0 = \bar{a}(t_{stop})$:

$$\bar{G} = G_0 + \frac{d\bar{G}(\bar{a}_0)}{d\bar{a}}(\bar{a} - \bar{a}_0), \tag{19}$$

where $G_0 = \bar{G}(\bar{a}_0)$ and $\frac{d\bar{G}(\bar{a}_0)}{d\bar{a}}$ can be computed from Eq. (7) and gives:

$$\frac{d\bar{G}(\bar{a}_0)}{d\bar{a}} = -\frac{4G_0}{\bar{a}_0}. \tag{20}$$

Replacing (19) and (20) into Eq. (3), we obtain:

$$\bar{v} = \chi' \exp\left(-\frac{4\alpha^2 G_0 \bar{a}}{\bar{a}_0 k_B T}\right) \tag{21}$$

with $\chi' = \chi \exp\left(\alpha^2 \frac{-\bar{G}_c + 5G_0}{k_B T}\right)$. The above equation integrates as:

$$\bar{a}(t) = \frac{k_B T \bar{a}_0}{4\alpha^2 G_0} \ln\left[\frac{4\chi' G_0 \alpha^2}{k_B T \bar{a}_0}(t - t_0) + \exp\left(\frac{4G_0\alpha^2}{k_B T}\right)\right], \tag{22}$$

where t_0 and $\bar{a}_0$ are the lower integration limits, corresponding to the initial time and position respectively where we consider the creep conditions to apply. The above expression can be simplified by setting $H_0 = \frac{(5G_0 - \bar{G}_c)\alpha^2}{k_B T}$, $\beta = \frac{5G_0 - \bar{G}_c}{4G_0}$ and introducing the characteristic time, $t^* = \frac{\beta \bar{a}_0}{H_0 \chi} \exp\left(-H_0(1 - 1/\beta)\right)$. It yields,

$$\bar{a}(t) - \bar{a}_0 = \frac{\bar{a}_0 \beta}{H_0} \ln\left[\frac{t - t_0}{t^*} + 1\right]. \tag{23}$$

At large times, when $t - t_0 \gg t^*$, the above equation reduces to

$$\bar{a}(t) - \bar{a}_0 \approx \frac{\bar{a}_0 \beta}{H_0} \ln\left(\frac{t - t_0}{t^*}\right), \tag{24}$$

$$\bar{v}(t) \approx \frac{\bar{a}_0 \beta}{H_0} \frac{1}{t - t_0}. \tag{25}$$

It is interesting to note for comparison, that in granular media logarithmic relaxation have also been observed [22] and that in rock mechanics Scholz [17] developed a simple model of creep in heterogeneous media where

the collective behavior resulting from local decreases of strength leads to a similar $\propto t^{-1}$ evolution of the deformation rate during the creep regime. We see that the form of Eq. (23) is similar to Eq.(1) which was used to described the evolution of the front in this relaxation regime in Fig. 4. It implies that Eq. (23) also provides a good description of the data and that our first order approximation appears to be valid in the range investigated in our experiments.

VII. CONCLUSIONS

We explored the average velocity of an interfacial crack under two different loading conditions. Both conditions induce crack velocities much lower than the Rayleigh wave velocity of the material either in the forced regime at imposed constant loading velocity, or in the relaxation regime. As often observed for homogeneous or weakly heterogeneous materials, the constant speed loading regime is compatible with a constant energy release rate and the relaxation regime is compatible with a time logarithmic deformation. The macroscopic evolution of the crack front is smooth and continuous, characteristic of creep processes. This is opposite to what is observed and modeled at the local scale, namely an intermittency of the fracture process which is described by a succession of local discrete brittle failures [1, 9]. Such "brittle-creep" behavior has been extensively studied in rocks where acoustic emissions are recorded during the otherwise slow global deformation of the sample (e.g. [17, 43, 54]) or in other materials like paper [13, 44, 55].

We developed a thermally activated fracture model that consists of a set of independent microscopic sites that break according to an Arrhenius law. The energy barrier is assumed to be a function of the difference between the local energy release rate G and the local critical energy release rate G_c. We show that for independent microscopic sites in time and space, the model reduces to a 1D model where the crack tip advance is controlled by the difference between the average energy release rate $\bar{G}$ and the average critical energy release rate $\bar{G_c}$. The model describes the fracturing process in the sub-critical regime close to the critical transition, *i.e.* the Griffith criterion $G = G_c$, as a mechanism only sensitive to the applied stress on the crack tip and the effective toughness of the material. It allows the crack propagation to be driven below the critical energy release rate by statistical stress fluctuations that trigger rupture at the scale of atomic bonds. We find that the typical length scale of the process is of the order of tens of picometer, in agreement with the value reported in *Ponson* [43] for rocks samples or in *Santucci et al.* [44] for paper. This suggests that the creeping mechanism we are observing is related to the breakage at the typical length scale of atomic bonds. Such an atomistic size is consistent with the framework showing that thermally activated rupture occurs at a characteristic size, at the level of single atomic bonds [13, 44]. It also suggests that stress fluctuations can trigger rupture of these atomic bonds. The length scale of this process, a few $10^{-11} - 10^{-10}$ m, is much smaller than the correlation length scale of the toughness heterogeneity of the material, which is typically of the order of the glass beads size used during peparation of the sample by blasting, of the order of 0.1-0.5 mm [51, 56].

We find that despite very different tested loading conditions, all experimental data of the macroscopic evolution of the crack can be well explained by the proposed sub-critical mechanism. Neglecting this temperature effect does not give a correct description of the crack propagation in a constant deflection regime during relaxation test. Moreover, several factors that would possibly influence the progression of the crack have been disregarded. They include possible mechanical finite rotation of the plate, viscoelastic flows inside the bulk of the PMMA plate like micro-bubbles, or chemical processes. However, despite these simplifications, the thermally activated model we propose, seems to correctly reproduce the evolution of the front during experiments over a large range of time scales (from 0.1 to more than 10000 s) and different loading paths, at least when the average advance of the front $\bar{a}$ is small compared to its initial position: this suggests that the neglected mechanisms have second order effects on the crack evolution compared to the stress induced creeping mechanism.

It is interesting to note that we reproduce the large scale evolution of the front propagation despite a simple description of the heterogeneous nature of the material. Indeed, the interface with spatially fluctuating toughness induced by the sandblasting procedure is represented for its macroscopic behavior by an average quantity. This might be due to the limited heterogeneity of the toughness when seen at a centimetric scale, as evidenced by the almost flat geometry of the crack front line (we never observed crack front distortions bigger than 10% of the system scale). This suggests that although heterogeneities are present and are encountered during the crack propagation, the macroscopic scale evolution is well described by the average energy release rate, which is an average quantity among all local sites. Such large scale information appears sufficient to predict the overall large-scale dynamics of the propagating crack under various loading regimes.

We acknowledge Alain Steyer for technical support. The project was supported by the French ANR RiskNat SUPNAF grant, by a CNRS french-norwegian PICS and an INSU CESSUR program. K.J.M. was partly supported by a visiting grant from Strasbourg University.

[1] K. J. Måløy, S. Santucci, J. Schmittbuhl, and R. Toussaint, Phys. Rev. Lett. **96** (2006).

[2] B. K. Atkinson, *Fracture Mechanics of Rocks* (Academic Press Inc., San Diego, Calif., 1991).

[3] E. Schulson and P. Duval, *Creep and Fracture of Ice* (Cambridge University Press, 2009).

[4] I. Smith, E. Landis, and G. M., *Fracture and Fatigue in Wood* (John Wiley & Sons Inc, 2003).

[5] T. L. Anderson, *Fracture mechanics - Fundamentals and applications* (CRC press, 1995), 2nd ed.

[6] B. Lawn, *Fracture of Brittle Solids* (Cambridge University Press, 1993), 2nd ed.

[7] L. Freund, *Dynamic fracture mechanics* (Cambridge University Press, 1990).

[8] J. Fineberg and M. Marder, Phys. Rep. **313**, 1 (1999).

[9] D. Bonamy, J. Phys. D: Appl. Phys. **42**, 214014 (2009).

[10] D. Unger, *Analytical fracture mechanics* (Dover Publications Inc, 1995).

[11] J. R. Rice, J. Mech. Phys. Solids **26**, 61 (1978).

[12] L. D. Landau and Lifshitz, *Statistical Physics, Part 1 (Third Edition)*, vol. 34 (1980).

[13] L. Vanel, S. Ciliberto, P.-P. Cortet, and S. Santucci, J. Appl. Physics D **42**, 214007 (2009).

[14] S. W. Freiman, J. Geophys. Res. **86**, 4072 (1984).

[15] S. M. Wiederhorn and L. H. Bolz, J. Am. Ceram. Soc. **53**, 543 (1970).

[16] R. J. Charles, Journal of Applied Physics **29**, 1549 (1958).

[17] C. H. Scholz, J. Geophys. Res. **73**, 3295 (1968).

[18] E. Favier, V. Lazarus, and J.-B. Leblond, in *Modern Practice in Stress and Vibration Analysis 2003 (MPSVA2003), University of Glasgow (GB)*, edited by M. S. Forum (Trans Tech Publications, Switzerland, 2003), vol. 440-441, pp. 153–160.

[19] N. Pindra, V. Lazarus, and J.-B. Leblond, J. Mech. Phys. Solids **58**, 281 (2010).

[20] V. Lazarus, J. Mech. Phys. Solids **59**, 121 (2011).

[21] S. N. Zhurkov, Int. J. of Fracture Mech **1**, 311 (1965).

[22] R. R. Hartley and R. P. Behringer, Nature **421**, 928 (2003).

[23] L. Bocquet, E. Charlaix, S. Ciliberto, and J. Crassous, Nature **396**, 735 (1998).

[24] G. Løvoll, K. J. Måløy, and E. G. Flekkøy, Phys. Rev. E.. **60**, 5872 (1999).

[25] M. Sahimi, *Heterogeneous materials II: Nonlinear and breakdown properties and atomistic modeling* (Springer-Verlag New York Inc, 2003).

[26] W. Weibull, J. Appl. Mech. **18**, 293 (1951).

[27] Z. Bažant, *Scaling of Structural Strength* (Butterworth-Heinemann Ltd, 2005), 2nd ed.

[28] A. B. Kolton, A. Rosso, T. Giamarchi, and w. Krauth, Phys. Rev. Lett. **97**, 057001 (2006).

[29] Z. Bažant and S. Pang, J. Mech. Phys. Solids **55**, 91 (2007).

[30] J. Obreimoff, Proc. R. Soc. Lond. **127**, 290 (1930).

[31] J. Schmittbuhl and K. J. Måløy, Phys. Rev. Lett. **78**, 3888 (1997).

[32] A. Delaplace, J. Schmittbuhl, and K. J. Måløy, Phys. Rev. E.. **60**, 1337 (1999).

[33] K. Tallakstad, R. Toussaint, S. Santucci, and K. J. Måløy, Phys. Rev. E (2011), in press.

[34] H. Gao and J. R. Rice, J. Appl. Mech. **56**, 828 (1989).

[35] J. Schmittbuhl, S. Roux, J.-P. Vilotte, and K. J. Måløy, Phys. Rev. Lett. **74**, 1787 (1995).

[36] S. Ramanathan and D. Fisher, Phys. Rev. B **58**, 6026 (1998).

[37] S. R. Pride and R. Toussaint, Physica A **312**, 159 (2002).

[38] R. Toussaint and S. R. Pride, Phys. Rev. E.. **71**, 046127 (2005).

[39] J. Schmittbuhl, A. Hansen, and G. G. Batrouni, Phys. Rev. Lett. **90** (2003).

[40] M. Alava, P. Nukalaz, and S. Zapperi, Adv. Phys. **55**, 349 (2006).

[41] S. Pradhan, A. Hansen, and B. Chakrabarti, Rev. Mod. Phys. **82**, 499 (2010).

[42] M. Grob, J. Schmittbuhl, R. Toussaint, L. Rivera, S. Santucci, and K. J. Måløy, Pure and Appl. Geophys. **166**, 777 (2009).

[43] L. Ponson, Phys. Rev. Lett. **103**, 055501 (2009).

[44] S. Santucci, L. Vanel, and S. Ciliberto, Phys. Rev. Lett. **93**, 095505 (2004).

[45] A. Saichev and D. Sornette, Phys. Rev. E.. **71**, 016608 (2005).

[46] P. Cortet, L. Vanel, and S. Ciliberto, Europhys. Lett. **74**, 602 (2006).

[47] R. Toussaint and S. R. Pride, Phys. Rev. E **66**, 036135 (2002).

[48] R. Toussaint and S. R. Pride, Phys. Rev. E **66**, 036136 (2002).

[49] R. Toussaint and S. R. Pride, Phys. Rev. E **66**, 036137 (2002).

[50] R. Toussaint and A. Hansen, Phys. Rev. E **73**, 046103 (2006).

[51] O. Lengliné, J. Schmittbuhl, J. Elkhoury, J.-P. Ampuero, R. Toussaint, and K. J. Måløy, submitted to J. Geophys. Res.

[52] A. B. Kolton, A. Rosso, and T. Giamarchi, Phys. Rev. Lett. **94**, 047002 (2005).

[53] D. Bonamy, S. Santucci, and L. Ponson, Phys. Rev. Lett. **101**, 045501 (2008).

[54] B. K. Atkinson, J. Geophys. Res. **89**, 4077 (1984).

[55] S. Santucci, L. Vanel, and S. Ciliberto, Eur. Phys. J Spec. Topics **146**, 341 (2007).

[56] S. Santucci, K. J. Måløy, R. Toussaint, and J. Schmittbuhl, in *Dynamics of Complex Interconnected Systems: Networks and Bioprocesses*, edited by A. T. Skjeltorp and A. V. Belushkin (Springer Netherlands, 2006), vol. 232 of *NATO Science Series II: Mathematics, Physics and Chemistry*, pp. 49–59, ISBN 978-1-4020-5030-5.